Applied Nanoscience
https://doi.org/10.1007/s13204-022-02689-y

ORIGINAL ARTICLE

Intensified Pb(II) adsorption using functionalized KCC-1 synthesized from rice husk ash in batch and column adsorption studies

R. Hasan[1] · **R. S. R. Mohd Zaki**[1] · **H. D. Setiabudi**[1,2] · **R. Jusoh**[1] · **A. A. Jalil**[3,4] · **M. Shokouhimehr**[5]

Received: 16 June 2022 / Accepted: 8 October 2022

Abstract

An attempt to investigate the feasibility of 3-aminopropyltriethoxysilane (3-APTES)-functionalized KCC-1 (NH_2/KCC-1) prepared from rice husk ash (RHA) for Pb(II) removal was executed. An effective functionalization of fibrous silica nanospheres (KCC-1) by NH_3 was confirmed by FTIR analysis. The optimized condition of Pb(II) adsorption in the batch system was at an initial Pb(II) concentration (X_1) of 307 mg/L, adsorbent dosage (X_2) of 2.43 g/L, and time (X_3) of 114 min, with the Pb(II) removal (Y) of 90.1% (predicted) and 91.2% (actual). NH_2/KCC-1 can be regenerated by nitric acid (0.1 M) with insignificant decline of Pb(II) removal percentage (adsorption = 91.2–67.3%, desorption = 77.7–51.9%) during 5 cycles adsorption–desorption study. The examination of column adsorption study at a varying flow rate (1–3 mL/min) and bed height (10–20 cm) showed a good performance at a lower flow rate and higher bed height. Both Adam–Bohalt model and Thomas model displayed a good correlation with experimental data. However, Thomas model was more suitable due to the high correlation coefficient, $R^2 = 0.91–0.99$. This study revealed the intensified Pb(II) adsorption using NH_2/KCC-1 synthesized from RHA in batch and column adsorption studies.

Keywords KCC-1 · Fibrous silica nanospheres · Pb(II) adsorption · Rice husk ash · Optimization

Introduction

Nowadays, due to the fast evolution of industrial development, environmental pollution has become one of the major concerns. The growth of the paper, batteries, tanneries, petrochemical, and fertilizer industries has directly or indirectly discharged heavy metals into the environment (Khan et al. 2021). Heavy metals are carcinogenic and have the potential to accumulate in living beings (Rehman et al. 2021).

Lead (Pb(II)) is known as the most poisonous and carcinogenic. Exposure to Pb(II) through inhalation and ingestion of food or water will cause severe diseases and permanent trauma to human's neurological system, deadly brain, kidney, and circulatory system (Rahman et al. 2019). Besides, Pb(II) can also affect aquatic life in physiology, biochemistry, behavior, and reproduction (Petitjean et al. 2019; El-Gendy et al. 2021). However, the maximum permissive limit (MPL) of Pb(II) concentration is only less than 0.5 µg/g, as itemized by World Health Organization (Loghmani et al. 2022). Therefore, the amount of Pb(II) emitted into the environment must be reduced because of its toxicity, even at modest levels of contamination.

R. Hasan and R. S. R. Mohd Zaki have equally contributed to this work.

✉ H. D. Setiabudi
herma@ump.edu.my

[1] Faculty of Chemical and Process Engineering Technology, College of Engineering Technology, Universiti Malaysia Pahang, Lebuhraya Tun Razak, 26300 Gambang, Kuantan, Pahang, Malaysia

[2] Centre for Research in Advanced Fluid and Processes, Universiti Malaysia Pahang, Lebuhraya Tun Razak, 26300 Gambang, Kuantan, Pahang, Malaysia

[3] School of Chemical and Energy Engineering, Faculty of Engineering, Universiti Teknologi Malaysia, 81310 Johor Bahru, Johor, Malaysia

[4] Centre of Hydrogen Energy, Institute of Future Energy, Universiti Teknologi Malaysia, 81310 Johor Bahru, Johor, Malaysia

[5] Department of Materials Science and Engineering, Research Institute of Advanced Materials, Seoul National University, Seoul 08826, Republic of Korea

The removal of Pb(II) has been examined using numerous techniques, for example, adsorption (Alqadami et al. 2020), chemical precipitation (Chen et al. 2018), membrane filtration (Jamshidifard et al. 2019), and ion exchange (Bezzina et al. 2019). Among these techniques, adsorption gained higher attraction due to its low cost, ability to minimize chemical and biological sludge, and flexible and straightforward design (Dotto and McKay 2020). However, selecting an appropriate adsorbent is critical to improving the adsorption process.

Mesoporous silica has attracted substantial attention as an adsorbent due to its variable pore size, wide surface area, and biocompatibility (Rechotnek et al. 2021). Lately, a new family of mesoporous silica, known as fibrous silica nanospheres (KCC-1), was introduced in 2010. KCC-1 features excellent characteristics, including nanosized, high surface area, large pore diameter, unprecedented fibrous surface morphology, hydrothermal stabilities, and high mechanical stabilities. Due to its excellent characteristics, KCC-1 has been explored in various applications, including dehydrogenation (Zhang et al. 2019), catalysis (Abdulrasheed et al. 2020), and drug delivery (Pishnamazi et al. 2021a; Follmann et al. 2020).

Additionally, previous studies proved that the KCC-1 has excellent potential for Pb(II) adsorption (Hasan and Setiabudi 2019). However, the cost for the manufacture of KCC-1 is high, which can be claimed on the cost of the silica source. Therefore, low cost and high availability of agricultural by-products with high silica content (Anuar et al. 2018; Hubadillah et al. 2018) will be a good choice. Rice husk is one of the major agricultural wastes with an annual production of 545 million metric tons (Mohseni et al. 2019), and has been demonstrated to have high silica composition after pyrolysis (Osman 2020). Therefore, employing rice husk ash (RHA) as an alternate silica source can be an excellent example of promoting the circular economy by converting low-value lignocellulosic materials into added-value products (Osman et al. 2020). This approach could also minimize solid waste pollution and consequently promote sustainable development.

Nevertheless, challenges arise when the performance of the silica materials synthesized from waste has low efficiency compared to commercial mesoporous silica. It has been reported that the efficiency of the adsorbent can be improved by surface modification of the adsorbent. Among others, 3-aminopropyltriethoxysilane APTES has been widely used as a surface modifier due to their possible interaction with the silanol group via siloxane bonds, electrostatic attraction, and hydrogen bonds (Cho et al. 2018). Therefore, in this research, KCC-1 synthesized from RHA was functionalized with an amino group to enhance the adsorption behavior of batch and column studies. To the best of the authors' knowledge, the current study is the first to explore the adsorption performance of amino-modified KCC-1 from RHA.

Materials and methods

Extraction of sodium silicate from rice husk ash (RHA)

The extraction process was conducted according to Hasan et al. (2019a). In brief, the rice husk ash (RHA) was washed and dried (120 °C, overnight) to remove impurities. Then, the mixture of RHA and sodium hydroxide (NaOH, Merck) was calcined (550 °C, 1 h) to prepare NaOH-fused RHA. The NaOH-fused RHA was mixed with deionized water, agitated (24 h), and filtered. The supernatant liquid was used for the KCC-1 preparation. According to the X-ray Fluorescence Spectrophotometry (XRF, Bruker S8 TIGER), SiO_2 was identified as a substantial component of RHA with a composition of 88.52%.

KCC-1 preparation

KCC-1 was synthesized consistent with Hasan et al. (2019b) with some modifications. Solution 1 [Na_2SiO_3-RHA, butanol (Merck), and toluene (Merck)] was mixed with Solution 2 [water, urea (Merck), and cetyltriammonium bromide (CTAB, Aldrich)], stirred (room temperature, 45 min), and heated (120 °C, 5 h) in a hydrothermal synthesis reactor. The mixture was centrifuged and filtered. The solid particles were oven-dried (100 °C, 12 h) and calcined (550 °C, 6 h) to obtain KCC-1.

Surface modification

KCC-1 was functionalized by mixing KCC-1 (3 g), toluene (50 mL), and 3-aminopropyltriethoxysilane (3-APTES) (2.4 g). The mixture was then refluxed (110 °C, 48 h) and filtered. The solid particles were then rinsed with ethanol and dried (100 °C, 12 h) to obtain NH_2/KCC-1.

Characterization

The crystallinity texture was analyzed by X-ray diffraction (XRD, Miniflex II Rigaku, 15 mA, 30 kV) with a Cu-Kα radiation ($\lambda = 1.54$ Å). The textural characteristics were studied using the Bruneuer–Emmett–Teller (BET, Micromeritics®) method at 77 K. Fourier-Transform Infrared (FTIR, Thermo Scientific Nicolet iS5) was conducted for functional groups investigation. Transmission Electron Microscopy (TEM, Leo Libra-120) was employed for morphology analysis. The specimen was sonicated in ethanol, and the solution was dropped onto an amorphous porous carbon grid.

Batch adsorption

A stock Pb(II) solution (1000 mg/L, $Pb(NO_3)_2$, Sigma-Aldrich) was prepared prior to dilution to the necessary concentration (50–400 mg/L). The NH_2/KCC-1 (0.5–5 g/L) was added to Pb(II) solution (200 mL, room temperature) while stirring for the adsorption process. The sample was collected at a specific time (0–140 min) and centrifuged (2 min, 3000 rpm). The Pb(II) concentration was determined using UV–Vis spectroscopy at 520 nm with a dithizone reagent.

The amount of Pb(II) adsorbed, and the percentage of Pb(II) removed were determined using Eqs. (1) and (2), respectively.

$$q_t = \left(\frac{C_o - C_t}{m}\right) \times V, \tag{1}$$

$$\text{Removal}\,(\%) = \left(\frac{C_o - C_t}{C_o}\right) \times 100, \tag{2}$$

where q_t (mg/g) signifies the quantity of Pb(II) adsorbed at a specific time, C_o (mg/L) represents the initial Pb(II) concentration, and C_t (mg/L) signifies the Pb(II) concentration at a specific time. V (L) represents the volume of the Pb(II) solution, and m (g) signifies the mass of NH_2/KCC-1.

Experimental design and optimization

Response Surface Methodology (RSM) (Statsoft Statistica 8.0) with a central composite design (CCD) was chosen as the experimental design. The independent variables were the initial concentration, X_1 (50–400 mg/L), adsorbent dosage, X_2 (0.5–5.0 g/L), and time, X_3 (0–140 min). These independent variables were selected according to the findings obtained from the one-factor-at-a-time method (OFAT). A total of 16 different trials were carried out in triplicate. The result was analyzed by applying the analysis of variance (ANOVA), coefficient of determination (R^2), and 3D response surface plots.

Column adsorption

Figure S1 depicts the column system, whereby KCC-1 and cotton wool were placed in the column as illustrated. Following that, glass beads were placed on both sides of the filter to ensure that the influent solution was distributed uniformly from top to bottom. Then, the column was washed with pure distilled water before being fed with a Pb(II) solution.

The continuous flow was used in the experiments, and the regular flow of the solution discharge volume was measured at specific times. 500 mL of a Pb(II)-containing solution was run through the column. At predefined intervals, samples were taken from the column output, followed by centrifugation and UV–vis analysis similar to the batch process.

Results and discussion

Characterization analysis

Figure 1a compares the FTIR spectra of KCC-1 and NH_2/KCC-1. From the graph, all materials showed the presence of a peak around 449 cm^{-1}, 797 cm^{-1}, 1058 cm^{-1}, and 3425 cm^{-1} that corresponded to Si–O bending, unsymmetrical stretching of Si–O, symmetrical Si–O, and O–H

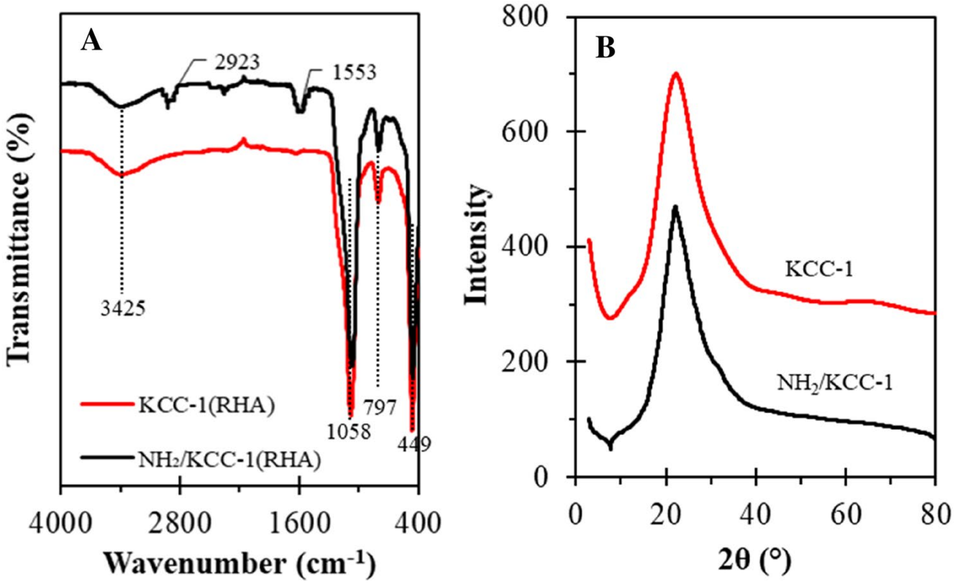

Fig. 1 **A** FTIR spectra and **B** XRD pattern of KCC-1 and NH_2/KCC-1

stretching vibration of Si–OH, respectively (Ershad et al. 2021). However, after surface modification with an amino group, addition peaks at 2923 cm^{-1} and 1553 cm^{-1} were detected that were ascribed as N–H stretching and N–H bending vibrations of the aminopropyl group, respectively. The presence of these peaks confirmed that the aminopropyl groups of 3-APTES were introduced into KCC-1. The presence of the amino group was also found by Zarei et al. (2019), who did a surface modification on KCC-1 and applied it to remove chromium.

Figure 1b displays the XRD pattern of KCC-1 and NH_2/KCC-1. The broad peaks at 20° and 30° proved the amorphous silica phase of the material (Hasan et al. 2019a). The XRD pattern showed no significant alterations, which suggested that the crystallinity texture of KCC-1 had not changed with the introduction of NH_2.

Figure 2a, b illustrates the TEM images of KCC-1 and NH_2/KCC-1, respectively. The synthesized KCC-1 is made up of uniform spheres with a fibrous morphology, similar to KCC-1 prepared from commercial silica sources, as reported by other researchers (Hitam et al. 2020; Zhang et al. 2019), indicating successful preparation of KCC-1 from RHA. The modification of KCC-1 with an amino group does not change the surface morphology of the KCC-1, as shown in Fig. 2b.

The BET analyses were employed to ascertain the surface area (SA_{BET}) and pore volume (V_p). The SA_{BET} of KCC-1 and NH_2/KCC-1 were 220 m^2/g and 224 m^2/g, respectively. NH_2/KCC-1 had a higher surface area, thus facilitating an effective adsorption process (Khantan et al. 2019). Notably, an increase in the V_p of 0.94 cm^3/g (KCC-1) to 1.12 cm^3/g (NH_2/KCC-1) allowed for high loadings of metals or non-metals pollutants.

Batch adsorption

Statistical analysis

Table 1 summarizes the 16 experimental runs with the response values (Pb(II) removal). The regression coefficient was decoded using multiple analyses, as shown in Eq. (3). In the equation, a positive and negative sign denotes synergistic and antagonistic effects, respectively.

$$\begin{aligned} Y = {} & 76.3648 + 0.0473X_1 + 2.1429X_2 + 0.0673\,X_3 \\ & - 0.0001X_1^2 - 0.4320X_2^2 - 0.0002X_3^2 \\ & - 0.0001X_1X_2 - 0.0001X_1X_2 - 0.0002X_2X_3, \end{aligned} \tag{3}$$

where Y is the estimated response, while $X_{1,}$ $X_{2,}$ and X_3 are the coded independent variables.

A comparison between the observed value (from the experiment) and predicted value (calculated from the regression model) of Pb(II) percentage removal is illustrated in Fig. S2. The good regression coefficient can be described with a close value of 1.0 or > 0.75 (Storm 2019). From the graph, the obtained high correlation coefficient, R^2 (0.9401), indicated that 94.01% of the data variability was considered for the model.

The understanding of the response surface quadratic model was further studied with variance analysis (ANOVA). ANOVA is a statistical tool that divides a collection of data into portions connected to specific sources of variation to test hypotheses associated with the model parameter (Jankovic et al. 2021). Table 2 lists the ANOVA data for this experiment. The tabulated F-value ($F_{table} = 4.10$) was lower than calculated F-value (F-model = 10.42) at 95% probability ($p = 0.05$), indicating a significant of the model.

The Pareto chart was utilized to determine which variable was significant in this model. The predicted effect of each independent variable was indicated as proportional length

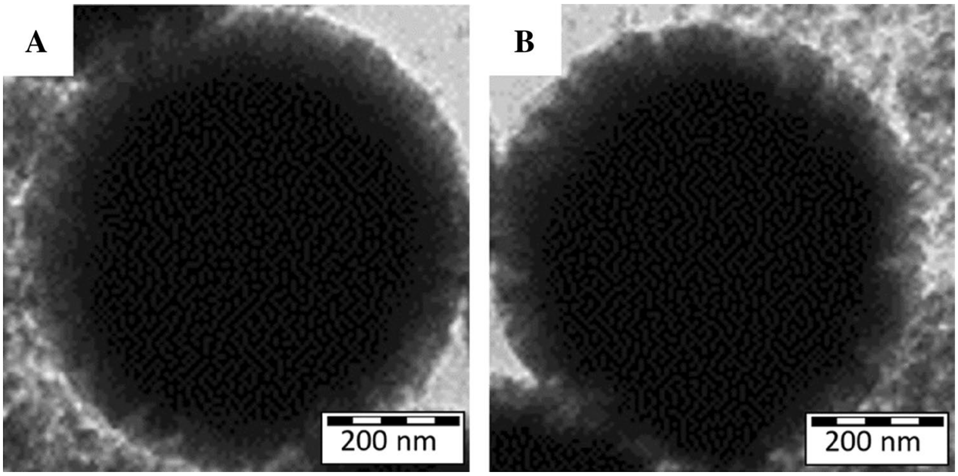

Fig. 2 TEM images of **A** KCC-1 and **B** NH_2/KCC-1

Table 1 Experimental design and experimental results of Pb(II) removal

Run	Independent variables						Response
	Initial concentration (mg/L), X_1		Adsorbent dosage (g/L), X_2		Time (min), X_3		Pb(II) removal (%), Y
	Uncoded	Coded	Uncoded	Coded	Uncoded	Coded	
1	50	− 1	0.5	− 1	60	− 1	82.99
2	50	− 1	0.5	− 1	180	1	86.28
3	50	− 1	5	1	60	− 1	81.77
4	50	− 1	5	1	180	1	84.91
5	400	1	0.5	− 1	60	− 1	87.92
6	400	1	0.5	− 1	180	1	86.75
7	400	1	5	1	60	− 1	86.54
8	400	1	5	1	180	1	85.31
9	50	− 1	2.75	0	120	0	85.09
10	400	1	2.75	0	120	0	89.78
11	225	0	0.5	− 1	120	0	87.38
12	225	0	5	1	120	0	86.63
13	225	0	2.75	0	60	− 1	88.66
14	225	0	2.75	0	180	1	88.63
15 (C)	225	0	2.75	0	120	0	90.81
16 (C)	225	0	2.75	0	120	0	90.49

Table 2 ANOVA for removal percentage of Pb(II)

Sources	Sum of square (SS)	Degree of freedom (*df*)	Mean square (MS)	*F*-value
Regression (SSR)	90.053	9	10.0	10.42
Residual	5.7411	6	0.96	
Total (SST)	95.794	15		

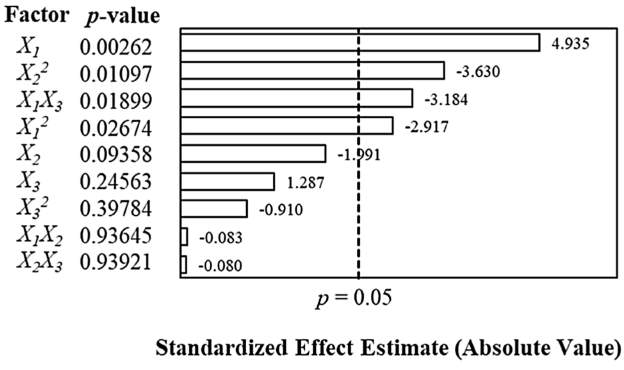

Fig. 3 Pareto chart for Pb(II) removal onto NH_2/KCC-1

corresponding to the absolute value, as illustrated using the horizontal bar chart shown in Fig. 3. The independent variables were examined using the *p*-value and *t*-value, in which the variables with a larger *t*-value magnitude or/and a lower *p*-value had a greater impact on the regression model (Setiabudi et al. 2013). The linear term of initial concentration (X_1), quadratic term of adsorbent dosage (X_2^2), interactive term between initial concentration and time (X_1X_3), and quadratic term of initial concentration (X_1^2), were statistically significant due to the large *t*-value magnitude and low *p*-value ($p < 0.05$). The other terms of the variables were regarded as less significant because of the larger *p*-value ($p > 0.05$). In short, initial concentration (X_1) had the greatest influence on Pb(II) removal, while the relation between adsorbent dose and time (X_2X_3) had the least.

Figure 4a depicts the interaction impacts of initial concentration (X_1) and time (X_3) on Pb(II) elimination. The elliptic form of the response surface demonstrated outstanding interaction amidst initial concentration and time. An increase in the initial concentration (from 50 to 300 mg/L) and time (from 40 to 100 min) increased the Pb(II) removal percentage until the optimum conditions ($X_1 = 300$–350 mg/L, $X_3 = 100$–150 min, $Y = 90\%$) were achieved, and decreased at elevated initial concentration (> 350 mg/L) and time (> 150 min). At the beginning of the time, the percentage removal increased with increasing time until it achieved the optimal (100–150 min) and continued to decrease at a higher time. This result can be clarified by a higher quantity of accessible active sites at the beginning of the time and decreases with increasing time. Additionally, when the initial concentration of Pb(II) increased, the percentage of Pb(II) removal increased as well, which was related to the sufficient active sites on the NH_2/KCC-1's surface to attract Pb(II) ions. However, after the adsorption on the active site

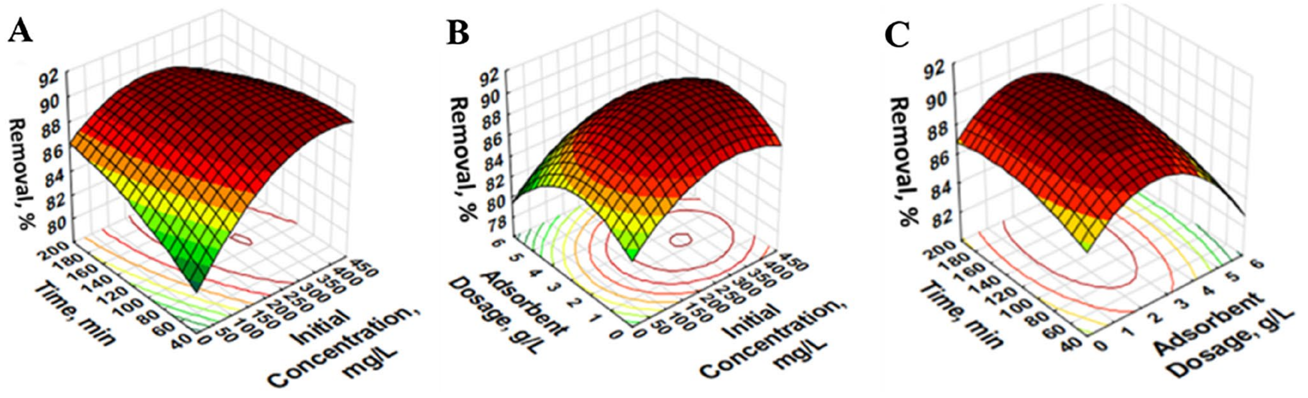

Fig. 4. 3D plots show the effects of **A** initial concentration and time, **B** initial concentration and adsorbent dosage, and **C** adsorbent dosage and time

achieved the saturated point, raising the initial concentration would not affect the Pb(II) removal.

The interaction impacts of initial concentration (X_1) and adsorbent dosage (X_2) on the elimination of Pb(II) are depicted in Fig. 4b. An increase in initial concentration and adsorbent dosage increased the removal of Pb(II) until it passed the optimum values around $X_1 = 300–350$ mg/L and $X_2 = 2–3$ g/L, respectively, with Pb(II) percentage removal around 90%, and declined at the elevated initial concentration (> 350 mg/L) and adsorbent dosage (> 3 g/L). This phenomenon increased the percentage removal of Pb(II) until a specific value. Then, it started to decrease as the formation of adsorbent aggregation reduced the viability of the active sites attached by Pb(II) ions (Ain et al. 2020). By comparing both independent variables, the initial concentration of Pb(II) displayed a more significant impact in Pb(II) removal than adsorbent dosage. This outcome was compatible with the Pareto chart analysis (Fig. 3), which indicated that the initial concentration had a higher *t*-value (4.935) than the adsorbent dosage with *t*-value of -1.991. A comparable result was described by Bahrami et al. (2019) for Pb(II) removal using starch phosphate. In their study, the Pb(II) removal improved with increasing initial Pb(II) concentration and adsorbent dosage, reaching the optimum at 63.57 mg/L and 0.25 g/L, respectively, but dropped at elevated values.

Figure 4c displays the impacts of adsorbent dosage (X_2) and time (X_3) on the elimination of Pb(II). According to the plot, increasing the adsorbent dosage and time concurrently increased the Pb(II) removal until it reached the optimum percentage (90%) at the adsorbent dosage of 2–3 g/L and time of 100–150 min, and then decreased as the adsorbent dosage and time were increased further. This finding can be explained by a higher quantity of accessible active sites at the beginning of the time and decreases with increasing time. Lingamdinne et al. (2018) reported a comparable trend for the Pb(II) adsorption using nickel ferrite-reduced graphene oxide (NFRGO) nanocomposite, in which the removal of Pb(II) increases with time and NFRGO dosage until the optimal condition was reached. It is interesting to note that NH_2/KCC-1 showed good adsorption performance owing to its exciting morphology that contains well-defined and ordered fibers coming out from the center of the particles and uniformly distributed in all directions. This advantage allows NH_2/KCC-1 to adsorb the pollutant more effectively.

The optimization modeling study suggested the optimal conditions were at initial Pb(II) concentration (X_1) of 307 mg/L, NH_2/KCC-1 dosage (X_2) of 2.43 g/L, and time (X_3) of 114 min, with Pb(II) removal (Y) of 90.1%. Triplicate experiments were conducted under optimal conditions to validate the optimization modeling findings. The removal of Pb(II) was attained at 91.2%, with a percentage error of 1.1%.

Kinetic study

In this study, three types of kinetic models [pseudo-first-order, pseudo-second-order (Ezzati 2020), and Elovich (Ealias and Saravanakumar 2018)] were utilized. The kinetics study was conducted at optimum conditions (NH_2/KCC-1 dosage of 2.43 g/L and time of 114 min) with different initial Pb(II) concentrations ($C_o = 100–500$ mg/L). The kinetics of heterogeneous chemisorption were characterized by the Elovich, while pseudo-first-order and pseudo-second-order defined adsorption behavior in physisorption and chemisorption, respectively (Nayak and Pal 2019). The equation of the models is expressed as follows:

$$\text{Pseudo - first - order:}\quad \log\left(q_e - q_t\right) = \log q_e - \frac{k_1}{2.303}t, \tag{4}$$

$$\text{Pseudo - second - order:}\quad \frac{t}{q_{\mathrm{t}}} = \frac{1}{k_2 q_{\mathrm{e}}^2} + \frac{1}{q_{\mathrm{e}}} t, \tag{5}$$

$$\text{Elovich:}\quad q_{\mathrm{e}} = \left(\frac{1}{\beta}\right) \ln(\alpha\beta) + \left(\frac{1}{\beta}\right) \ln t, \tag{6}$$

where the quantities of Pb(II) adsorbed at time, *t,* and equilibrium represent as q_{t} (mg/g) and q_{e} (mg/g), respectively. k_1 (L/min) represents pseudo-first-order's rate constant, while k_2 (g/mg·min) represents pseudo-second-order's rate constant. α (mg/(g min)) signifies adsorption rate constant, and β (g/mg) represents desorption constant.

The linear regression coefficient (R^2) and other parameters are tabulated in Table 3. The tabulated data was the average value of triplicate experiments. Hence, the pseudo-second-order model was the best-fitted isotherm attributable to the highest R^2 (≥ 0.9986) and the closest value of q_{e}. In contrast, the Elovich model was the weakest due to the lowest R^2 value. The pseudo-second-order model also best fitted the Pb(II) adsorption onto common Guar gum/bentonite bionanocomposites (Ahmad and Mirza 2018), as well as in our previous study for Pb(II) adsorption using KCC-1 (Hasan et al. 2019a). In a nutshell, the Pb(II) adsorption onto NH_2/KCC-1 is a chemisorption process, and the adsorption rate is proportionate to the accessibility of the active sites on the NH_2/KCC-1's surface.

Isotherm study

The isotherm models of Freundlich (Al-Ghouti and Da'ana 2020), Temkin (Aharoni and Ungarish 1977), Dubinin-Radushkevich (Dubinin 2002), and Langmuir (Langmuir 2002) were utilized in this study. The isotherm study was conducted at optimum conditions (NH_2/KCC-1 dosage of 2.43 g/L and time of 114 min) with different initial Pb(II) concentrations ($C_{\mathrm{o}} = 100$–500 mg/L). Temkin is employed to examine how adsorbent–adsorbate interactions influence the adsorption process (Liu et al. 2020). Meanwhile, the Dubinin–Radushkevich is accredited to the heterogeneous surface assumption theory for the adsorption mechanism. In contrast, Langmuir and Freundlich explained that monolayer adsorption happens on the homogenous adsorbent's surface and multilayer adsorption over the heterogeneous adsorbent's surface, respectively (Benkaddour et al. 2018). The linearized forms of these isotherms were expressed as the following equations.

$$\text{Langmuir:}\quad \frac{C_{\mathrm{e}}}{q_{\mathrm{e}}} = \frac{1}{q_{\mathrm{m}} K_{\mathrm{L}}} + \frac{C_{\mathrm{e}}}{q_{\mathrm{m}}}, \tag{7}$$

$$\text{Freundlich:}\quad \log q_{\mathrm{e}} = \log K_{\mathrm{F}} + \frac{1}{n} \log C_{\mathrm{e}}, \tag{8}$$

$$\text{Temkin:}\quad q_{\mathrm{e}} = B \ln A + B \ln C, \tag{9}$$

$$\text{Dubinin} - -\text{Radushkevich:}\quad \ln q_{\mathrm{e}} = \ln q_{\mathrm{m}} - K_{\mathrm{DR}}\, \varepsilon^2, \tag{10}$$

where q_{e} (mg/g) represents the equilibrium adsorption capacity, while the maximum adsorption capacity is symbolized as q_{m} (mg/g). n is an empirical constant, C_{e} (mg/L) is the Pb(II) concentration at equilibrium, while K_{L} (L/mg) and K_{F} ((mg/g) (L/mg)$^{1/n}$)) are the Langmuir and Freundlich constant, respectively. For the Temkin isotherm, B represents Temkin constant, while an equilibrium binding constant is symbolized as A (L/g). For the Dubinin–Radushkevich isotherm, K_{DR} (mol^2/kJ^2) represents Dubinin–Radushkevich constant, while Polanyi potential is symbolized as ε (J/mol). ε can be calculated from $\varepsilon = RT \ln(1 + 1/C_{\mathrm{e}})$, where R (J/mol·K) is gas constant and T (K) is the absolute temperature. The Langmuir equilibrium parameter ($R_{\mathrm{L}} = 1/(1 + K_{\mathrm{L}} C_{\mathrm{o}})$) is used to indicates the isotherm shape either irreversible, favorable, linear, or unfavorable, for $R_{\mathrm{L}} = 0$, $0 < R_{\mathrm{L}} < 1$, $R_{\mathrm{L}} = 1$, or $R_{\mathrm{L}} > 1$, respectively [44].

Table 4 lists the computed parameters for the studied models. The tabulated data was the average value of triplicate experiments. Thus, the Langmuir isotherm

Table 3 Kinetic parameters for removal of Pb(II) onto NH_2/KCC-1

Models	Parameter	100 ppm	200 ppm	300 ppm	400 ppm	500 ppm
Experimental	$q_{\mathrm{e,exp}}$ (mg/g)	41.237	42.779	51.143	52.836	54.734
Pseudo-first-order	$q_{\mathrm{e,cal}}$ (mg/g)	6.2661	9.4842	9.8175	9.3240	10.678
	k_1 (min^{-1})	0.0392	0.0343	0.0309	0.0161	0.0306
	R^2	0.8888	0.9853	0.9845	0.8767	0.9939
Pseudo-second-order	$q_{\mathrm{e,cal}}$ (mg/g)	41.494	43.668	51.813	53.191	55.249
	k_2 (g/mg min)	0.0189	0.0092	0.0087	0.0070	0.0084
	R^2	0.9999	0.9998	0.9997	0.9986	0.9998
Elovich kinetic	α (mg/(g min))	2E+09	3E+07	4E+08	8E+08	2E+08
	β (g/mg)	0.6263	0.5060	0.4713	0.4774	0.4241
	R^2	0.9295	0.8795	0.9363	0.9068	0.9269

Table 4 Isotherm models for Pb(II) adsorption onto NH_2/KCC-1

Isotherm	Parameters	Value
Langmuir	q_m (mg/g)	28.169
	K_L (L/mg)	0.0749
	R^2	0.9927
	R_L	0.1178
Freundlich	n	1.5083
	K_f (mg/g) $(L/mg)^{1/n}$	488.65
	R^2	0.9309
Temkin	B (J/mol)	31.312
	A (L/g)	154.95
	R^2	0.9223
Dubinin-Radushkevich	q_m (mg/g)	58.621
	K_{ad} (10^{-4})	1
	R^2	0.9898

was the best-fitted model attributable to the highest value of R^2, which indicated that Pb(II) uptake occurs on the homogenous surface by monolayer adsorption. The Langmuir's q_m value, K_L constant, R_L value was 28.169 mg/g, 0.0749 L/mg, and 0.1178, respectively. The observed results verified that the synthesized NH_2/KCC-1 considerably favored the Pb(II) adsorption with Pb(II) initial concentration = 307 mg/L, adsorbent dosage of NH_2/KCC-1 = 2.43 g/L, and time = 114 min. Furthermore, by comparing the maximum adsorption capacity (q_m) of NH_2/KCC-1 (this study) with KCC-1 synthesized from RHA (Hasan et al. 2019a), NH_2/KCC-1 has a higher q_m (28.169 mg/g) than the KCC-1 (26.954 mg/g), indicated an excellent performance of NH_2/KCC-1 in removing Pb(II). The excellent performance of NH_2/KCC-1 can be explained by the positive role of amino groups in improving the surface area and functional groups that responsible in the adsorption process.

The q_m value for NH_2/KCC-1 (this study) was compared to the q_m values reported in the literature for various silica adsorbents, as shown in Table S1. It was noticed that NH_2/KCC-1 has a superior adsorption capacity, which is attributed to the exceptional physicochemical features (nanosized, high surface area, large pore diameter, and unprecedented fibrous surface morphology), showing the considerable potential of NH_2/KCC-1. Interestingly, NH_2/KCC-1 was produced using RHA as a silica source, which benefited environmental impacts.

Reusability study

Figure 5 depicts the performance of NH_2/KCC-1 over five adsorption–desorption experiments at optimum conditions (Pb(II) concentration of 307 mg/L, NH_2/KCC-1 dosage of 2.43 g/L, and time of 114 min). The desorption method was studied using a chemical treatment of nitric acid (HNO_3) (0.1 M) because of its effectivity, as published by Place et al. (2018). The adsorption–desorption displayed a decreasing pattern with an increasing number of cycles. This finding could be due to the blockage of the active sites by Pb(II) molecules and changes in the adsorbent's structure and the chemical composition after the adsorption process (Fu et al. 2019). Abdelrahman and Hegazey (2019) reported a similar phenomenon for adsorption–desorption cycles of Pb(II) removal by hydroxy sodalite/chitosan composites.

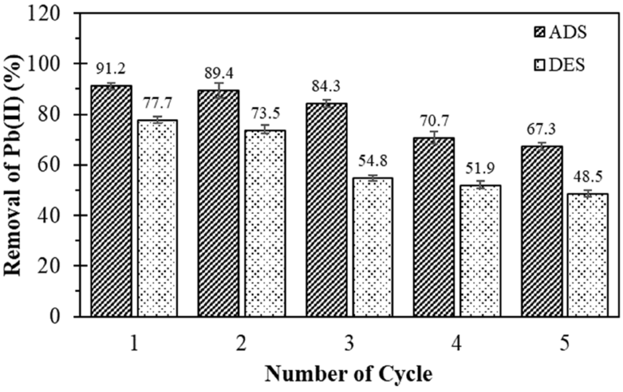

Fig. 5 Regeneration and reusability of NH_2/KCC-1

Even though the adsorption–desorption showed a decreasing pattern, the percentage reduction was less significant (3.4%) as compared to Pb(II) removal by KCC-1, almost 7% for the fifth cycle, as described in our earlier publication (Hasan et al. 2019a). Additionally, the efficacy of KCC-1 toward Pb(II) adsorption and Pb(II) desorption was lower than NH_2/KCC-1, with percentage differences of 19.3% and 4.8%, respectively. The better performance of

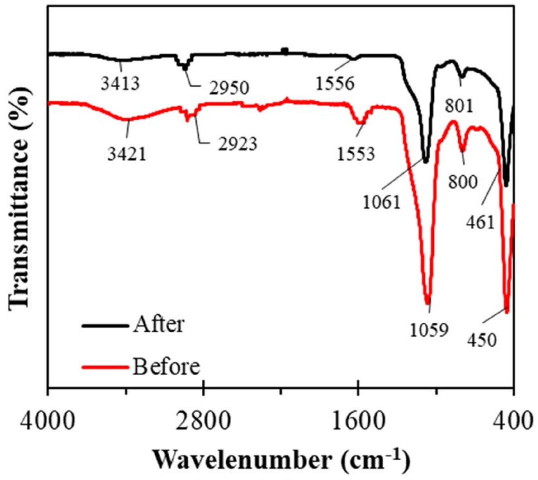

Fig. 6 FTIR spectra of NH_2/KCC-1 before and after Pb(II) adsorption

NH_2/KCC-1 compared to KCC-1 could be ascribed to the positive role of the amine group in the adsorption process.

The FTIR spectra of NH_2/KCC-1 (before and after adsorption) revealed identical infrared peaks, as illustrated in Fig. 6. However, the peak intensity had altered after adsorption. Both FTIR spectra showed the existence of O–H stretching vibration of Si–OH (3421 cm^{-1} and 3413 cm^{-1}), stretching vibration of N–H (2923 cm^{-1} and 2950 cm^{-1}), bending vibration of N–H (1553 cm^{-1} and 1556 cm^{-1}), symmetrical stretching of Si–O (1059 cm^{-1} and 1061 cm^{-1}), unsymmetrical stretching of Si–O (800 cm^{-1} and 801 cm^{-1}), and Si–O bending (450 cm^{-1} and 461 cm^{-1}), respectively (Pishnamazi et al. 2021b). After adsorption, the peaks were shifted to a higher wavenumber, attributable to the electrostatic interaction, complexation, and coordination of functional groups with metal ions (Shahabuddin et al. 2018). The amino and hydroxyl groups are implicated in Pb(II) adsorption by surface complexation (Wu et al. 2019).

Column adsorption

Effect of flow rate

The impact of flow rates at a fixed value of bed height (15 cm) and initial Pb(II) concentration (307 mg/L) was illustrated by the breakthrough curve in Fig. 7a. With increasing flow rate, the plotted curve showed a reduction in residence time and adsorption capacity. Therefore, the adsorption process can be considered the most effective at lower flow rates due to the higher residence time, leading to higher Pb(II) elimination from an aqueous phase. Bo and their team (Bo et al. 2020) conducted the adsorption of Pb^{2+} in batch and column systems using amine (N/O)-enrichment of adsorbent ($CM_{0.5}AP_{0.75}$). Their research showed that insufficient contact between $CM_{0.5}AP_{0.75}$ and Pb^{2+} in a higher flow rate resulted in decreasing adsorption capacity. Consequently, employing a lower flow rate was recommended for the system to achieve high adsorption of Pb^{2+}.

Effect of bed height

The influence of column bed height was examined with a fixed initial Pb(II) concentration (307 mg/L) and flow rate (1 mL/min). The result of the continuous study is shown in Fig. 7b. From the graph, the adsorption capacity and breakthrough curve showed that increasing bed height (from 10 to 20 cm) increased the adsorption capacity and sharpened the breakthrough curve shape. The quantity of adsorbent in the column affected the Pb(II) removal. Besides, Pb(II) solution spent more time in contact with the adsorbent, and an enormous number of active sites were accessible when a higher/more extended bed height was used.

Adsorption modeling

The adsorption modeling was examined using the Adam–Bohart model and Thomas model. The linearised forms of these models are expressed as the following equations.

$$\text{Adam - Bohart model:}\quad \ln\left(\frac{C_t}{C_o}\right) = K_{AB}C_o t - \frac{K_{AB}N_o Z}{U_o}, \tag{11}$$

$$\text{Thomas model:}\quad \ln\left(\frac{C_o}{C_t} - 1\right) = \frac{K_{Th}q_o m}{Q} - k_{Th}C_o t, \tag{12}$$

where C_o (mg/L) and C_t (mg/L) represent inlet and outlet Pb(II) concentration, respectively. t (min) represents the time

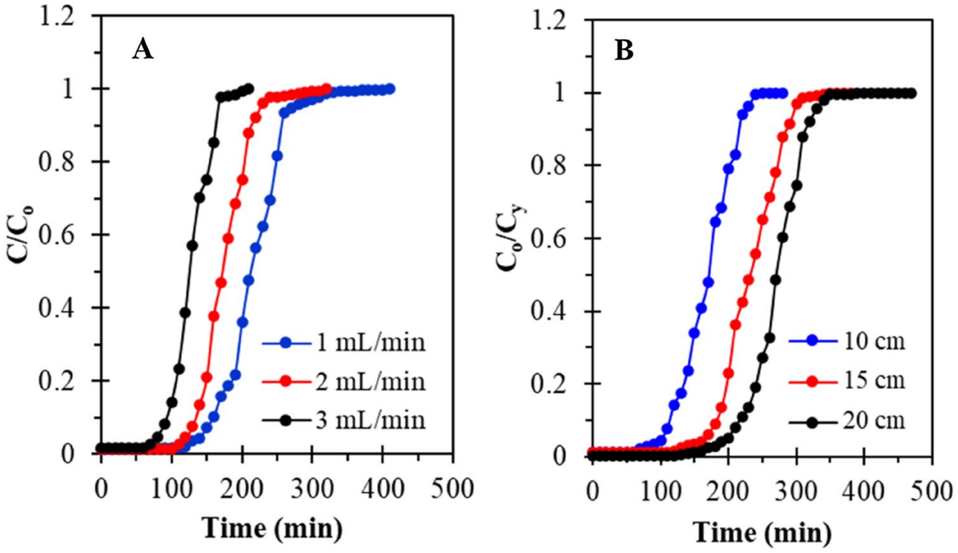

Fig. 7 Effect of **A** flow rate and **B** adsorbent height on continuous removal of Pb(II) onto NH_2/KCC-1

of the breakthrough, Z (cm) signifies the column height, Q (mL/min) represents flow rate, and N_o (mg/L) indicates saturation concentration. Meanwhile, K_{AB} (L/mg min) and K_{Th} (mL/min mg) represent the kinetic constant of the Adam–Bohart and Thomas models, respectively.

Adam–Bohart model explained the theory about surface reaction, and the equilibrium was assumed not instantaneously. Therefore, the reaction rate was proportionate to the remaining fraction of adsorption capacity on the adsorbent. To study this model, the graph of $\ln(C_t/C_o)$ versus t (not shown) was plotted, and the calculated parameter from Eq. (11) is tabulated in Table 5. The obtained data indicated that the value of K_{AB} reduced with an increment in an inlet Pb(II) concentration, whereas the value of N_o increased with an increment in the inlet Pb(II) concentration. This result indicated that, at initial column adsorption, the external mass transfer had dominated the overall kinetic system (Zhang et al. 2018). In addition, the Adam–Bohalt model provided a comprehensive and straightforward approach to analyzing column adsorption. However, this model was valid in a limited range of conditions used. Besides, the R^2 was also relatively low, which was between 0.91 and 0.98.

Thomas model has been extensively utilized in explaining the performance of the column adsorption process because this model assumes the internal and external diffusions will not be the limiting step. The graph of $\ln((C_o/C_t)\text{-}1)$ versus t was plotted (not shown), and the calculated parameter from the graph is shown in Table 5. According to the findings, as the inlet Pb(II) concentration increased, the K_{Th} value decreased, while q_o increased. This phenomenon happened as a result of the driving force effect between Pb(II) attached to the NH$_2$/KCC-1's surface and Pb(II) in solution at different inlet concentrations, thus increasing the q_o value. Besides, the R^2 was also high, which was between 0.91 and 0.99. Therefore, the Thomas model was more suitable to describe this column adsorption. Zhao et al. (2020) also reported the same for Pb(II) adsorption onto MOFs-DHAQ.

Conclusion

This study successfully functionalized KCC-1 derived from rice husk ash (RHA) with an amino group to produce NH$_2$/KCC-1. According to response surface methodology (RSM), the optimal condition was discovered to be at an initial Pb(II) concentration (X_1) of 307 mg/L, adsorbent dosage (X_2) of 2.43 g/L, and time (X_3) of 114 min, with Pb(II) removal (Y) of 90.1% (predicted) and 91.2% (actual). The Pareto chart revealed that the significant effect was an initial Pb(II) concentration (X_1), while the minor effect was the interaction between adsorbent dosage and time ($X_2\ X_3$). NH$_2$/KCC-1 had the prospect of being employed in multiple cycles with adsorption performance of (91.2–67.3%) and desorption performance of (77.7–51.9%). According to the column adsorption study, the adsorption process showed good performance at a lower flow rate (1 mL/min) and higher bed height (20 cm). Additionally, the adsorption process was well-fitted Thomas model, and was presented by a high correlation coefficient (R^2) of 0.91 to 0.99. In summary, the NH$_2$/KCC-1 adsorbent performed well in Pb(II) adsorption and was effectively used in both batch and column adsorption systems. The successful preparation of NH$_2$/KCC-1 derived from RHA significantly revealed the ability of agricultural wastes as a silica precursor, which could minimize solid waste pollution and promote sustainable development. With these advantages, further studies can be conducted to discover the effectiveness of other silica-rich solid wastes as silica's precursors in synthesizing KCC-1 or other mesoporous silica families.

Table 5 The parameter of Adam–Bohalt and Thomas models

Adam–Bohalt model

C_o (mg/L)	Z (cm)	Q (mL/min)	U_o (cm/min)	K_{AB} (L/mg min)	N_o (mg/L)	R^2
100	30	1	0.1111	2.40E−05	64.1985	0.9193
200	30	1	0.1111	1.83E−05	78.9556	0.9885
300	30	1	0.1111	1.11E−05	164.5113	0.9360
400	30	1	0.1111	8.40E−06	548.6678	0.9430
500	30	1	0.1111	5.30E−06	642.9420	0.9384

Thomas model

C_o (mg/L)	m (g)	Q (mL/min)	K_{Th} (mL/min mg)	q_o (mg/g)	R^2	C_o (mg/L)
100	2.1	1	4.5251E−05	834.50	0.9176	100
200	2.1	1	3.0270E−05	8145.80	0.9911	200
300	2.1	1	1.2570E−05	12,781.65	0.9393	300
400	2.1	1	1.0101E−05	44,123.07	0.9520	400
500	2.1	1	7.2277E−06	29,292.21	0.9390	500

Supplementary Information The online version contains supplementary material available at https://doi.org/10.1007/s13204-022-02689-y.

Acknowledgements The financial assistance provided by Universiti Malaysia Pahang through International Publication Grant (RDU203303) and Postgraduate Research Grant (PGRS210316) are acknowledged.

Declarations

Conflict of interest There is no conflict of interest.

References

Abdelrahman EA, Hegazey RM (2019) Utilization of waste aluminum cans in the fabrication of hydroxysodalite nanoparticles and their chitosan biopolymer composites for the removal of Ni(II) and Pb(II) ions from aqueous solutions: kinetic, equilibrium, and reusability studies. Microchem J 145:18–25. https://doi.org/10.1016/J.MICROC.2018.10.016

Abdulrasheed AA, Jalil AA, Hamid MYS, Siang TJ, Fatah NAA, Izan SM, Hassan NS (2020) Dry reforming of methane to hydrogen-rich syngas over robust fibrous KCC-1 stabilized nickel catalyst with high activity and coke resistance. Int J Hydrog Energy 45(36):18549–18561. https://doi.org/10.1016/J.IJHYDENE.2019.04.126

Aharoni C, Ungarish M (1977) Kinetics of activated chemisorption part 2—theoretical models. J Chem Soc 73:456–464. https://doi.org/10.1039/F19777300456

Ahmad R, Mirza A (2018) Synthesis of Guar gum/bentonite a novel bionanocomposite: isotherms, kinetics and thermodynamic studies for the removal of Pb(II) and crystal violet dye. J Mol Liq 249:805–814. https://doi.org/10.1016/J.MOLLIQ.2017.11.082

Ain QU, Zhang H, Yaseen M, Rasheed U, Liu K, Subhan S, Tong Z (2020) Facile fabrication of hydroxyapatite–magnetite–bentonite composite for efficient adsorption of Pb(II), Cd(II), and crystal violet from aqueous solution. J Clean Prod 247:119088. https://doi.org/10.1016/J.JCLEPRO.2019.119088

Al-Ghouti MA, Da'ana DA (2020) Guidelines for the use and interpretation of adsorption isotherm models: a review. J Hazard Mater 393:122383. https://doi.org/10.1016/J.JHAZMAT.2020.122383

Alqadami AA, Naushad M, AlOthman ZA, Alsuhybani M, Algamdi M (2020) Excellent adsorptive performance of a new nanocomposite for removal of toxic Pb(II) from aqueous environment: adsorption mechanism and modeling analysis. J Hazard Mater 389:121896. https://doi.org/10.1016/J.JHAZMAT.2019.121896

Anuar MF, Fen YW, Zaid MHM, Matori KA, Khaidir REM (2018) Synthesis and structural properties of coconut husk as potential silica source. Results Phys 11:1–4. https://doi.org/10.1016/J.RINP.2018.08.018

Bahrami M, Amiri MJ, Bagheri F (2019) Optimization of the lead removal from aqueous solution using two starch based adsorbents: design of experiments using response surface methodology (RSM). J Environ Chem Eng 7(1):102793. https://doi.org/10.1016/J.JECE.2018.11.038

Benkaddour S, Slimani R, Hiyane H, el Ouahabi I, Hachoumi I, el Antri S, Lazar S (2018) Removal of reactive yellow 145 by adsorption onto treated watermelon seeds: kinetic and isotherm studies. Sustain Cham Pharm 10:16–21. https://doi.org/10.1016/J.SCP.2018.08.003

Bezzina JP, Ruder LR, Dawson R, Ogden MD (2019) Ion exchange removal of Cu(II), Fe(II), Pb(II) and Zn(II) from acid extracted sewage sludge—resin screening in weak acid media. Water Res 158:257–267. https://doi.org/10.1016/J.WATRES.2019.04.042

Bo S, Luo J, An Q, Xiao Z, Wang H, Cai W, Zhai S, Li Z (2020) Efficiently selective adsorption of Pb(II) with functionalized alginate-based adsorbent in batch/column systems: mechanism and application simulation. J Clean Prod 250:119585. https://doi.org/10.1016/J.JCLEPRO.2019.119585

Chen Q, Yao Y, Li X, Lu J, Zhou J, Huang Z (2018) Comparison of heavy metal removals from aqueous solutions by chemical precipitation and characteristics of precipitates. J Water Process Eng 26:289–300. https://doi.org/10.1016/J.JWPE.2018.11.003

Cho M, Park J, Yavuz CT, Jung Y (2018) A catalytic role of surface silanol groups in CO_2 capture on the amine-anchored silica support. Phys Chem Chem Phys 20(17):12149–12156. https://doi.org/10.1039/C7CP07973G

Dotto GL, McKay G (2020) Current scenario and challenges in adsorption for water treatment. J Environ Chem Eng 8(4):103988. https://doi.org/10.1016/J.JECE.2020.103988

Dubinin MM (2002) The potential theory of adsorption of gases and vapors for adsorbents with energetically nonuniform surfaces. Chem Rev 60(2):235–241. https://doi.org/10.1021/CR60204A006

El-Gendy KS, Gad AF, Radwan MA (2021) Physiological and behavioral responses of land molluscs as biomarkers for pollution impact assessment: a review. Environ Res 193:110558. https://doi.org/10.1016/J.ENVRES.2020.110558

Elias M, Saravanakumar MP (2018) Facile synthesis and characterisation of AlNs using protein rich solution extracted from sewage sludge and its application for ultrasonic assisted dye adsorption: isotherms, kinetics, mechanism and RSM design. J Environ Manage 206:215–227. https://doi.org/10.1016/J.JENVMAN.2017.10.032

Ershad ZS, Shadjou N, Mahmoudian M, Ahour F (2021) Polyphenylsulfone membrane modified by novel dendritic fibrous nanosilica (KCC-1-*n*Pr-NH-AcCys) toward water treatment. J Environ Chem Eng 9(4):105329. https://doi.org/10.1016/J.JECE.2021.105329

Ezzati R (2020) Derivation of pseudo-first-order, pseudo-second-order and modified pseudo-first-order rate equations from Langmuir and Freundlich isotherms for adsorption. Chem Eng J 392:123705. https://doi.org/10.1016/J.CEJ.2019.123705

Follmann HDM, Oliveira ON, Martins AC, Lazarin-Bidóia D, Nakamura CV, Rubira AF, Silva R, Asefa T (2020) Nanofibrous silica microparticles/polymer hybrid aerogels for sustained delivery of poorly water-soluble camptothecin. J. Colliod Interface Sci 567:92–102. https://doi.org/10.1016/J.JCIS.2020.01.110

Fu W, Wang X, Huang Z (2019) Remarkable reusability of magnetic Fe_3O_4-encapsulated $C_3N_3S_3$ polymer/reduced graphene oxide composite: a highly effective adsorbent for Pb and Hg ions. Sci Total Environ 659:895–904. https://doi.org/10.1016/J.SCITOTENV.2018.12.303

Hasan R, Setiabudi HD (2019) Removal of Pb(II) from aqueous solution using KCC-1: optimization by response surface methodology (RSM). J King Saud Univ Sci 31(4):1182–1188. https://doi.org/10.1016/j.jksus.2018.10.005

Hasan R, Chong CC, Bukhari SN, Jusoh R, Setiabudi HD (2019a) Effective removal of Pb(II) by low-cost fibrous silica KCC-1 synthesized from silica-rich rice husk ash. J Ind Eng Chem 75:262–270. https://doi.org/10.1016/j.jiec.2019.03.034

Hasan R, Chong CC, Setiabudi HD (2019b) Synthesis of KCC-1 using rice husk ash for Pb removal from aqueous solution and petrochemical wastewater. Bull Chem React 14(1):196–204. https://doi.org/10.9767/bcrec.14.1.3619.196-204

Hitam CNC, Jalil AA, Izan SM, Azami MS, Hassim MH, Chanlek N (2020) The unforeseen relationship of Fe_2O_3 and ZnO on fibrous silica KCC-1 catalyst for fabricated *Z*-scheme extractive-photooxidative desulphurization. Powder Technol 375:397–408. https://doi.org/10.1016/J.POWTEC.2020.07.114

Hubadillah SK, Othman MHD, Ismail AF, Rahman MA, Jaafar J, Iwamoto Y, Honda S, Dzahir MIHM, Yusop MZM (2018) Fabrication of low cost, green silica based ceramic hollow fibre membrane prepared from waste rice husk for water filtration application. Ceram Int 44(9):10498–10509. https://doi.org/10.1016/J.CERAMINT.2018.03.067

Jamshidifard S, Koushkbaghi S, Hosseini S, Rezaei S, Karamipour A, Jafari rad A, Irani M (2019) Incorporation of UiO-66-NH_2 MOF into the PAN/chitosan nanofibers for adsorption and membrane filtration of Pb(II), Cd(II) and Cr(VI) ions from aqueous solutions. J Hazard Mater 368:10–20. https://doi.org/10.1016/J.JHAZMAT.2019.01.024

Jankovic A, Chaudhary G, Goia F (2021) Designing the design of experiments (DOE)—an investigation on the influence of different factorial designs on the characterization of complex systems. Energy Build 250:111298. https://doi.org/10.1016/J.ENBUILD.2021.111298

Khan FSA, Mubarak NM, Tan YH, Khalid M, Karri RR, Walvekar R, Abdullah EC, Nizamuddin S, Mazari SA (2021) A comprehensive review on magnetic carbon nanotubes and carbon nanotube-based buckypaper for removal of heavy metals and dyes. J Hazard Mater 413:125375. https://doi.org/10.1016/J.JHAZMAT.2021.125375

Khantan N, Shadjou N, Hasanzadeh M (2019) Synthesize of dendritic fibrous nano-silica functionalized by cysteine and its application as advanced adsorbent. Nanocomposites 5(4):104–113. https://doi.org/10.1080/20550324.2019.1669925

Langmuir I (2002) The constitution and fundamental properties of solids and liquids. Part I. Solids. J Am Chem Soc 38(11):2221–2295. https://doi.org/10.1021/JA02268A002

Lingamdinne LP, Koduru JR, Chang YY, Karri RR (2018) Process optimization and adsorption modeling of Pb(II) on nickel ferrite-reduced graphene oxide nano-composite. J Mol Liq 250:202–211. https://doi.org/10.1016/J.MOLLIQ.2017.11.174

Liu Y, Xiong Y, Xu P, Pang Y, Du C (2020) Enhancement of Pb(II) adsorption by boron doped ordered mesoporous carbon: isotherm and kinetics modeling. Sci Total Environ 708:134918. https://doi.org/10.1016/J.SCITOTENV.2019.134918

Loghmani M, Tootooni MM, Sharifian S (2022) Risk assessment of trace element accumulation in two species of edible commercial fish *Scomberoides commersonnianus* and *Cynoglossus arel* from the northern waters of the Oman Sea. Mar Pollut Bull 174:113201. https://doi.org/10.1016/J.MARPOLBUL.2021.113201

Mohseni E, Kazemi MJ, Koushkbaghi M, Zehtab B, Behforouz B (2019) Evaluation of mechanical and durability properties of fiber-reinforced lightweight geopolymer composites based on rice husk ash and nano-alumina. Constr Build Mater 209:532–540. https://doi.org/10.1016/J.CONBUILDMAT.2019.03.067

Nayak AK, Pal A (2019) Development and validation of an adsorption kinetic model at solid–liquid interface using normalized gudermannian function. J Mol Liq 276:67–77. https://doi.org/10.1016/J.MOLLIQ.2018.11.089

Osman AI (2020) Mass spectrometry study of lignocellulosic biomass combustion and pyrolysis with NO_x removal. Renew Energy 146:484–496. https://doi.org/10.1016/J.RENENE.2019.06.155

Osman AI, Farrell C, Al-Muhtaseb AH, Harrison J, Rooney DW (2020) The production and application of carbon nanomaterials from high alkali silicate herbaceous biomass. Sci Rep 10(1):1–13. https://doi.org/10.1038/s41598-020-59481-7

Petitjean Q, Jean S, Gandar A, Côte J, Laffaille P, Jacquin L (2019) Stress responses in fish: from molecular to evolutionary processes. Sci Total Environ 684:371–380. https://doi.org/10.1016/J.SCITOTENV.2019.05.357

Pishnamazi M, Hafizi H, Pishnamazi M, Marjani A, Shirazian S, Walker GM (2021a) Controlled release evaluation of paracetamol loaded amine functionalized mesoporous silica KCC1 compared to microcrystalline cellulose based tablets. Sci Rep 11(1):1–11. https://doi.org/10.1038/s41598-020-79983-8

Pishnamazi M, Khan A, Kurniawan TA, Sanaeepur H, Albadarin AB, Soltani R (2021b) Adsorption of dyes on multifunctionalized nano-silica KCC-1. J Mol Liq 338:116573. https://doi.org/10.1016/J.MOLLIQ.2021.116573

Place BK, Young CJ, Ziegler SE, Edwards KA, Salehpoor L, VandenBoer TC (2018) Passive sampling capabilities for ultra-trace quantitation of atmospheric nitric acid (HNO_3) in remote environments. Atmos Environ 191:360–369. https://doi.org/10.1016/J.ATMOSENV.2018.08.030

Rahman MM, Hossain KFB, Banik S, Sikder MT, Akter M, Bondad SEC, Rahaman MS, Hosokawa T, Saito T, Kurasaki M (2019) Selenium and zinc protections against metal-(loids)-induced toxicity and disease manifestations: a review. Ecotoxicol Environ Saf 168:146–163. https://doi.org/10.1016/J.ECOENV.2018.10.054

Rechotnek F, Follmann HDM, Silva R (2021) Mesoporous silica decorated with L-cysteine as active hybrid materials for electrochemical sensing of heavy metals. J Environ Chem Eng 9(6):106492. https://doi.org/10.1016/J.JECE.2021.106492

Rehman AU, Nazir S, Irshad R, Tahir K, ur Rehman K, Islam RU, Wahab Z (2021) Toxicity of heavy metals in plants and animals and their uptake by magnetic iron oxide nanoparticles. J Mol Liq 321:114455. https://doi.org/10.1016/J.MOLLIQ.2020.114455

Setiabudi HD, Jalil AA, Triwahyono S, Kamarudin NHN, Jusoh R (2013) Ir/Pt-HZSM5 for *n*-pentane isomerization: effect of Si/Al ratio and reaction optimization by response surface methodology. Chem Eng J 217:300–309. https://doi.org/10.1016/j.cej.2012.12.011

Shahabuddin S, Tashakori C, Komboh MA, Setoudehniakarrani Z, Saidur R, Nodeh HR, Bidhendi ME (2018) Kinetic and equilibrium adsorption of lead from water using magnetic metformin-substituted SBA-15. Environ Sci Technol. https://doi.org/10.1039/C7EW00552K

Storm K (2019) Introduction to construction statistics using excel. In: Industrial process plant construction estimating and man-hour analysis, 1st edn. Gulf Professional Publishing, Oxford, pp 1–21

Wu D, Wang Y, Li Y, Wei Q, Hu L, Yan T, Feng R, Yan L, Du B (2019) Phosphorylated chitosan/$CoFe_2O_4$ composite for the efficient removal of Pb(II) and Cd(II) from aqueous solution: adsorption performance and mechanism studies. J Mol Liq 277:181–188. https://doi.org/10.1016/J.MOLLIQ.2018.12.098

Zarei F, Marjani A, Joshaghani AH (2019) Triamino-anchored KCC-1: a novel and promising adsorbent for fast and highly effective aqueous CrVI removal. J Environ Chem Eng 7(5):103309. https://doi.org/10.1016/J.JECE.2019.103309

Zhang Y, Jin F, Shen Z, Lynch R, Al-Tabbaa A (2018) Kinetic and equilibrium modelling of MTBE (methyl tert-butyl ether) adsorption on ZSM-5 zeolite: batch and column studies. J Hazard Mater 347:461–469. https://doi.org/10.1016/J.JHAZMAT.2018.01.007

Zhang S, Qian Y, Ahn WS (2019) Catalytic dehydrogenation of formic acid over palladium nanoparticles immobilized on fibrous mesoporous silica KCC-1. Chinese J Catal 40(11):1704–1712. https://doi.org/10.1016/S1872-2067(19)63303-6

Zhao J, Wang C, Wang S, Zhou Y (2020) Experimental and DFT study of selective adsorption mechanisms of Pb(II) by UiO-66-NH_2 modified with 1,8-dihydroxyanthraquinone. J Ind Eng Chem 83:111–122. https://doi.org/10.1016/J.JIEC.2019.11.019